

Post-Perovskite Phase Transition in the Pyrolitic Lowermost Mantle: Implications for Ubiquitous Occurrence of Post-Perovskite Above CMB

Kei Hirose¹, Yasuhiro Kuwayama², Laura Cobden³, Mayu Kusakabe², Shigehiko Taten¹, and Yasuo Ohishi⁴

¹Tokyo Institute of Technology

²The University of Tokyo

³Utrecht University

⁴Japan Synchrotron Radiation Research Institute

November 22, 2022

Abstract

We conducted X-ray diffraction (XRD) measurements of a pyrolitic mantle material up to 4480 K at 122-166 GPa in a laser-heated diamond-anvil cell (DAC). Results demonstrate that the phase transition between bridgmanite and post-perovskite occurs in pyrolite within the lowermost mantle pressure range even at >4000 K. It suggests the ubiquitous occurrence of post-perovskite above the core-mantle boundary (CMB), which may be consistent with recent high-quality seismology data that non-observations of D'' reflections are exceptions. Combining with earlier experiments performed at and below the normal lower-mantle geotherm, our data show that the bridgmanite + post-perovskite two-phase region is ~ 5 GPa thick and the Clapeyron slope of the boundary is $+7(+2/-3)$ MPa/K in agreement with previous theoretical calculations. The global presence of rheologically weak post-perovskite at the bottom of the mantle has profound implications in seismology, geodynamics, and heat transfer from the core.

1 **Post-Perovskite Phase Transition in the Pyrolitic Lowermost Mantle:** 2 **Implications for Ubiquitous Occurrence of Post-Perovskite Above CMB**

3 Yasuhiro Kuwayama¹, Kei Hirose^{1,2}, Laura Cobden³, Mayu Kusakabe¹, Shigehiko
4 Tateno², and Yasuo Ohishi⁴

5
6 ¹Department of Earth and Planetary Science, The University of Tokyo, Tokyo, Japan

7 ²Earth-Life Science Institute, Tokyo Institute of Technology, Tokyo, Japan

8 ³Department of Earth Sciences, Utrecht University, Utrecht, The Netherlands

9 ⁴Japan Synchrotron Radiation Research Institute, SPring-8, Hyogo, Japan

10 **Key Points:**

- 11 • We conducted synchrotron XRD measurements of a pyrolitic mantle material up to
12 4480 K at 122–166 GPa in a laser-heated diamond-anvil cell.
- 13 • Phase transition between bridgmanite and post-perovskite occurs in pyrolite within
14 the lowermost mantle pressure range even at >4000 K.
- 15 • Ubiquitous occurrence of post-perovskite above the CMB is consistent with recent
16 high-quality seismological observations of D'' reflections.

17 **Abstract** We conducted X-ray diffraction (XRD) measurements of a pyrolitic mantle
18 material up to 4480 K at 122–166 GPa in a laser-heated diamond-anvil cell (DAC).
19 Results demonstrate that the phase transition between bridgmanite and post-perovskite
20 occurs in pyrolite within the lowermost mantle pressure range even at >4000 K. It
21 suggests the ubiquitous occurrence of post-perovskite above the core-mantle boundary
22 (CMB), which may be consistent with recent high-quality seismology data that non-
23 observations of D'' reflections are exceptions. Combining with earlier experiments
24 performed at and below the normal lower-mantle geotherm, our data show that the
25 bridgmanite + post-perovskite two-phase region is ~5 GPa thick and the Clapeyron slope
26 of the boundary is $+7_{-3}^{+2}$ MPa/K in agreement with previous theoretical calculations. The
27 global presence of rheologically weak post-perovskite at the bottom of the mantle has
28 profound implications in seismology, geodynamics, and heat transfer from the core.

29 **Plain Language Summary** (Al, Fe)-bearing MgSiO₃ bridgmanite is a predominant
30 mineral in the lower mantle. While bridgmanite with MgSiO₃ end-member composition
31 is known to undergo a phase transition to post-perovskite at lowermost mantle pressures,

32 the pressures and thickness of the phase boundary in a typical mantle material (pyrolite)
33 have been controversial. The present synchrotron XRD measurements of pyrolite
34 performed up to 4480 K around the CMB pressure show that the bridgmanite/post-
35 perovskite phase transition takes place within the lowermost mantle pressure range even
36 under high temperatures of the CMB region. The bridgmanite + post-perovskite two-
37 phase region is found to be about 90 km thick. These results suggest the global presence
38 of post-perovskite above the CMB, which is consistent with recent seismological
39 observations of D'' reflectors not only in the circum-Pacific high velocity regions but also
40 in many areas away from subduction zones. Post-perovskite is rheologically weak, and
41 its ubiquitous occurrence in the lowermost mantle has important seismological and
42 geodynamical implications. The high positive pressure/temperature slope ($+7_{-3}^{+2}$ MPa/K)
43 of the boundary suggests that a phase transition to bridgmanite assists upwelling of
44 plumes from hot regions above the CMB.

45 1. Introduction

46 Both experiments and theory have shown that a phase transition between bridgmanite
47 (perovskite-type structure) and post-perovskite occurs in MgSiO₃ end-member under the
48 lowermost mantle conditions (~120 GPa and ~2400 K), where the D'' seismic velocity
49 discontinuity is observed (Murakami et al., 2004; Oganov & Ono, 2004; Tateno et al.,
50 2009). The Clapeyron slope of the phase boundary in MgSiO₃ was determined to be +8–
51 13 MPa/K, several times larger in magnitude than those of major upper mantle phase
52 transitions. The pressures and sharpness of the post-perovskite phase transition have been
53 examined also in a pyrolitic mantle material. In a natural mantle, Al and Fe impurities
54 (e.g., Tateno et al., 2005; Mao et al., 2005; Hirose et al., 2008; Catalli et al., 2009) and
55 the coexistence with ferropericlase (Sinmyo et al., 2011) affect the transition pressure and
56 broaden a pressure interval of transition (see a review by Hirose et al., 2015). It has been
57 repeatedly reported the post-perovskite phase transition occurs in a pyrolitic lowermost
58 mantle around 120 GPa, comparable to the case in pure MgSiO₃, along the normal lower-
59 mantle geotherm with a ~5 GPa pressure interval (Murakami et al., 2005; Ono & Oganov,
60 2005; Ohta et al., 2008). On the other hand, the similar XRD study by Grocholski et al.
61 (2012) found higher transition pressure that is beyond the pressure range of the Earth's
62 mantle and much broader pressure interval (140–168 GPa at 2500 K).

63 In these previous experimental studies on pyrolite, however, the stabilities of bridgmanite
64 and post-perovskite have been explored only up to 2700 K under the lowermost mantle
65 conditions. There are more observations of the D'' seismic discontinuity in seismically

66 fast regions associated with paleo-subduction than in slow regions—although this may
67 be influenced by favorable earthquake source and receiver combinations—and in some
68 locations the D” discontinuity is not observed at all (see reviews by Wyssession et al.,
69 1998, Cobden et al., 2015, and Jackson & Thomas, 2021). The high Clapeyron slope of
70 the bridgmanite to post-perovskite phase transition might suggest that bridgmanite is
71 stable (post-perovskite is absent) to the CMB in relatively hot areas. Even in cold regions,
72 “paired” discontinuities (positive S-wave velocity jump at the D” discontinuity and
73 negative one at a deeper level near the CMB) might indicate the presence of bridgmanite
74 above the CMB, instead of post-perovskite, as a consequence of back transformation from
75 post-perovskite to bridgmanite at high temperatures in a thermal boundary layer (a
76 double-crossing scenario) (Thomas et al., 2004; Hernlund et al., 2005). It is of great
77 importance to verify these scenarios by phase equilibria experiments on multi-phase
78 assemblages that are representative of average mantle material under high temperatures
79 of the CMB region. In addition, the Clapeyron slope of the bridgmanite/post-perovskite
80 boundary was determined to be +5 to +13 MPa/K in MgSiO₃ end-member by theories
81 (Tsuchiya et al., 2004; Oganov & Ono, 2004) and experiments (Ono & Oganov, 2005;
82 Hirose et al., 2006; Tateno et al., 2009). It is several times larger in magnitude than those
83 of major upper mantle phase transitions, suggesting that the post-perovskite transition has
84 important dynamical consequences (Nakagawa & Tackley, 2004; Tackley et al., 2007).
85 The high positive Clapeyron slope was reported also for pyrolite, but it was constrained
86 by experiments performed in narrow temperature ranges less than ~1000 K (Ono &
87 Oganov, 2005; Ohta et al., 2008; Grocholski et al., 2012).

88 Here we performed synchrotron XRD measurements of a pyrolitic mantle material to
89 investigate the post-perovskite phase transition at high temperatures (3570 K and higher)
90 including those above its solidus temperature. The results show that bridgmanite/post-
91 perovskite phase transition occurs within the lowermost pressure range even at >4000 K.
92 Combining with the earlier experimental results by Ohta et al. (2008), the post-perovskite-
93 in and bridgmanite-out curves are constrained by data obtained in a wide temperature
94 range from 1780 to 4480 K, and the Clapeyron slope is found to be $+7_{-3}^{+2}$ MPa/K when
95 the gold pressure scale proposed by Fei et al. (2007) is applied. These results suggest that
96 post-perovskite is present globally above the CMB, which may be consistent with recent
97 high-quality seismological data that non-observations of D” reflection are exceptional
98 (Jackson & Thomas, 2021).

99 2. Experimental Methods

100 High-pressure and -temperature (P - T) experiments were performed with *in-situ* XRD
101 measurements in a laser-heated DAC. We employed a symmetric-type DAC with beveled
102 90- μm culet diamond anvils. A starting material was the same as that used in Ohta et al.
103 (2008); it was prepared from gel with the chemical composition of a natural peridotite
104 KLB-1, similar to pyrolite (Takahashi, 1986). The sample was mixed with fine gold
105 powder and loaded into a hole at the center of a pre-indented rhenium gasket. Argon was
106 cryogenically loaded and used as a thermal insulator.

107 After compression, heating was performed from both sides of the sample using a couple
108 of 100 W single-mode Yb fiber lasers (SPI Lasers Co. Ltd.) with beam shaping optics
109 that converts a beam with a Gaussian intensity distribution to one with a flat-top
110 distribution. The laser spot size was approximately 30 μm across. Heating duration was
111 3 sec. One-dimensional radial temperature profile across a hot spot was obtained by a
112 spectro-radiometric method (e.g., Tateno et al., 2018a) (Figure 1). In runs #1–3 in which
113 the sample was partially molten, temperature shown in Table 1 corresponds to that at the
114 boundary between a melt pool and a solid layer, which was determined by a combination
115 of the temperature profile and a melting texture found in a cross section of a recovered
116 sample (e.g., Hasegawa et al., 2021). For subsolidus experiments (runs #4 and #5), sample
117 temperatures are the average in a 6 μm region at the hot spot, from which XRD data were
118 collected. The overall temperature uncertainty may be $\pm 5\%$ according to Mori et al.
119 (2017). The sample was heated only once in each run. Pressure at high temperature was
120 determined based on the unit-cell volume of gold (Fei et al., 2007). Those in the earlier
121 experiments performed by Ohta et al. (2008) were based on the equation of state (EoS)
122 of gold proposed by Hirose et al. (2008), which is not applicable at high temperatures like
123 ~ 4000 K. Therefore, we recalculated the pressures in Ohta et al. (2008) using the Mie-
124 Grüneisen-Debye EoS of gold proposed by Fei et al. (2007), in order to compare their
125 results with those obtained in this study (Table 1).

126 Angle-dispersive XRD patterns were collected *in-situ* at high P - T at the beamline
127 BL10XU, SPring-8 synchrotron radiation facility (Hirao et al., 2020) (Figure 2). A
128 monochromatic incident X-ray beam was focused by stacked compound refractive lenses
129 and collimated to approximately 6 μm area (full width at half maximum) on a sample.
130 The wavelength was 0.4133 to 0.4158 \AA (~ 30 keV). XRD data were obtained
131 continuously during heating on a digital flat panel X-ray detector (Perkin Elmer) with
132 exposure time of 1 sec. To obtain conventional 1D diffraction patterns, 2D XRD images
133 were integrated as a function of 2θ angle (Seto et al., 2010).

134 After high P - T experiments, samples in runs #1–3 were recovered from a DAC, and their
135 cross sections across the center of a laser-heated spot were prepared parallel to the
136 compression axis by using a focused Ga ion beam (FIB) (FEI, Versa3D DualBeam). X-
137 ray elemental maps were obtained with an energy-dispersive X-ray spectrometry (EDS)
138 attached with a field-emission-type scanning electron microscope (FE-SEM) in the dual
139 beam FIB system (Figure 1).

140 3. Results

141 We have conducted five separate high P - T experiments on a pyrolitic mantle material up
142 to 156 GPa and 3570 K (Table 1). In order to avoid kinetic hindering of phase
143 transformation especially in such a multi-component system, heating was made on an
144 amorphous starting material at a single P - T condition in each run. In run #1, the sample
145 was compressed and then heated to 3910 K at 122 GPa, higher than the solidus
146 temperature of pyrolite (Nomura et al., 2014; Kim et al., 2020) (Figure 3a). The XRD
147 spectrum collected *in-situ* during heating shows that bridgmanite and minor post-
148 perovskite, in addition to ferropericlase and CaSiO_3 perovskite, grew from the amorphous
149 sample (Figure 2a). Microprobe analyses of the cross section of this sample recovered
150 from high pressure demonstrate that there is a round pocket of quenched melt at the center,
151 being enriched in Fe and Ca and depleted in Si (Figure 1). This melt pocket is surrounded
152 by a Si-rich and (Fe, Ca)-poor layer, which should represent bridgmanite (\pm post-
153 perovskite) observed in the high P - T XRD pattern. It indicates that bridgmanite is the
154 liquidus phase, consistent with the earlier melting experiments on pyrolite performed by
155 Tateno et al. (2014).

156 Similar experiments were made in runs #2 and #3 at conditions slightly higher in both P
157 and T (Figure 3a). Diffuse scattering signals from melt are recognized in their *in-situ*
158 XRD patterns (Fiquet et al., 2010), in particular for run #2 (Figure 2b). The XRD data
159 indicate that melt coexisted with bridgmanite and minor ferropericlase (post-perovskite
160 is absent) in run #2 at 128 GPa and 4480 K. In contrast, the high P - T XRD pattern is
161 dominated by post-perovskite in run #3 performed at 130 GPa and 4300 K (Figure 2c).
162 In addition, runs #4 and #5 were conducted at 156–166 GPa and 3570–3860 K under
163 subsolidus conditions (Figure 3a), which is supported by observations that the number of
164 peaks and their relative intensities in XRD patterns did not change upon quenching
165 temperature.

166 These results of runs #1–3 tightly constrain the post-perovskite-in and bridgmanite-out
167 conditions around 4000 K (Figure 3a). While partial melts coexisted with both

168 bridgmanite and post-perovskite in runs #1 and 3, either one of them was dominant in
169 these experiments (Figures 2a and 2c), indicating that their P - T conditions should be close
170 to the post-perovskite-in and bridgmanite-out curves, respectively. The width of the post-
171 perovskite phase transition should thus be about 5 GPa, corresponding to a lowermost
172 mantle depth range of 90 km, similar to that observed by Ohta et al. (2008) at lower
173 temperatures below 2550 K. When combined with Ohta et al. (2008)'s data (Table 1), our
174 results obtained in a wide temperature range from 1780 to 4480 K at 108–130 GPa show
175 the Clapeyron slope of these post-perovskite-in and bridgmanite-out curves to be $+7_{-3}^{+2}$
176 MPa/K, although the slope should change at the solidus curve (Figure 3a).

177 4. Discussion

178 4.1. Post-Perovskite Phase Transition in Pyrolitic Lowermost Mantle

179 Both the pressure (~ 120 GPa at 2400 K) and Clapeyron slope of the post-perovskite phase
180 transition boundary we obtained for pyrolite are in agreement with those for MgSiO_3 end-
181 member reported by earlier *ab initio* calculations (Tsuchiya et al., 2004; Oganov & Ono,
182 2004). While the experiments on pyrolite carried out by Grocholski et al. (2012) found
183 the phase transition at 140–168 GPa and 2500 K, earlier XRD measurements including
184 those by another group have repeatedly demonstrated that it takes place around 120 GPa
185 (Murakami et al., 2005; Ono & Oganov, 2005; Ohta et al., 2008) along the normal lower-
186 mantle geotherm (Brown & Shankland, 1981). Such a large discrepancy is not reconciled
187 with the difference in pressure scale employed to determine experimental pressures in
188 these studies, although pressure estimates can change as much as 15 GPa in the relevant
189 pressure range, depending on choices of an internal pressure standard and its equation of
190 state (see a review by Hirose et al., 2015) (Figure 3b). The difference in a pressure
191 medium is also unlikely to be an important source of the discrepancy; noble gas (argon
192 or neon) pressure medium was used in Ono & Oganov (2005) and this study as well as in
193 Grocholski et al. (2012).

194 The Clapeyron slope of $+7_{-3}^{+2}$ MPa/K depends on the choice of the Au pressure scale.
195 When different EoSs of gold (Jamieson et al., 1982; Anderson et al., 1989; Shim et al.,
196 2002; Tsuchiya, 2003) other than the Fei et al. (2007)'s EoS are employed, the slope
197 becomes smaller ranging from +3 to +7 MPa/K (Figure 3b). The pressures of the
198 transition also becomes lower. The slope of $+7_{-3}^{+2}$ MPa/K found in pyrolite is markedly
199 smaller than $+13 \pm 1$ MPa/K in MgSiO_3 (Tateno et al., 2009), which could be because of
200 the effects of Al and Fe impurities included in natural samples.

201 The present experiments and the earlier ones by Ohta et al. (2008) demonstrate that
202 bridgmanite and post-perovskite coexist in a pyrolitic mantle material in a ~5 GPa
203 pressure interval at ~4000 K and ~2000–2500 K, respectively (Figure 3a). The thickness
204 of the bridgmanite + post-perovskite two-phase region has been reported to be wider,
205 more than 20 GPa in (Al, Fe)-bearing MgSiO₃ (Catalli et al., 2009; Andraut et al., 2010).
206 Nevertheless, bridgmanite/post-perovskite coexists with (Mg,Fe)O ferropericlase in
207 pyrolite, and the partitioning of FeO with ferropericlase results in lower FeO
208 concentration in post-perovskite than in bridgmanite. It leads to a much narrower
209 bridgmanite + post-perovskite two-phase region in pyrolite than that in the (Al, Fe)-
210 bearing MgSiO₃ system (Sinmyo et al., 2011) as observed in this study as well as in Ohta
211 et al. (2008).

212 4.2. Ubiquitous Occurrence of Post-Perovskite above CMB

213 These results show that post-perovskite transforms into bridgmanite above 4800 K at the
214 CMB (Figure 3). It is much higher than the present-day CMB temperature, while its
215 estimates range from 3600 to 4300 K (e.g., Lay et al., 2008; Nomura et al., 2014; Kim et
216 al., 2020). If the deep lower mantle is dominated by a pyrolitic material, it suggests that
217 1) the bridgmanite/post-perovskite phase transition takes place globally in the lowermost
218 mantle although the transition is not sharp, and 2) post-perovskite is present ubiquitously
219 above the CMB. This conclusion does not depend on the choice of the EoS of gold to
220 determine experimental pressures (Figure 3b). If the lower mantle is not pyrolitic but
221 more enriched in silica and therefore poor in (Mg,Fe)O ferropericlase (Murakami et al.,
222 2012; Mashino et al., 2020), the *P-T* location of the post-perovskite-in curve does not
223 change as long as the chemical composition of bridgmanite is similar (Figure 3a), while
224 the bridgmanite + post-perovskite two-phase coexisting region should be wider (Sinmyo
225 et al., 2011).

226 The ~5 GPa pressure width of the bridgmanite + post-perovskite coexistence corresponds
227 to ~90 km depth interval in the lowermost mantle. The sharpness of the D'' seismic
228 discontinuity should be less than this (Weber et al., 1996) and potentially as narrow as 8–
229 30 km (i.e. <2 GPa) (Lay & Young, 1989; Lay, 2008; Wyssession et al., 1998), suggesting
230 that the bridgmanite/post-perovskite transition boundary in pyrolite may not be observed
231 as a seismic velocity discontinuity as argued by Lay (2008).

232 The D'' discontinuity is found mainly in high-velocity regions underneath the circum-
233 Pacific (Wyssession et al., 1998; Cobden et al., 2015; Jackson & Thomas, 2021), and this

234 has been attributed to the enrichment in subducted depleted mantle materials (harzburgitic
235 rocks), in which the bridgmanite to post-perovskite phase transition occurs in a narrow
236 pressure range because they are poor in Al and Fe impurities (Grocholski et al., 2012). D''
237 seismic reflections could also be produced in these regions by scattering off chemical
238 heterogeneities (e.g., Cobden & Thomas, 2013). On the other hand, there are observations
239 of the D'' discontinuity beneath the central Pacific as well (Lay et al., 2006; Cobden &
240 Thomas, 2013; Jackson & Thomas, 2021). Post-perovskite should be predominant above
241 the CMB including such areas away from the circum-Pacific high-velocity regions. Our
242 results do not preclude the bridgmanite/post-perovskite transition in pyrolite from
243 generating D'' reflections; stress-induced re-equilibration within the two-phase region can
244 produce high amplitude seismic reflections, even when the transition region is thick
245 (Langrand et al., 2019). Additionally, development of the lattice-preferred orientation of
246 post-perovskite may generate sharp reflectors within a broad two-phase region (Ammann
247 et al., 2010; Pisconti et al., 2019).

248 Indeed, the ubiquitous occurrence of post-perovskite above the CMB has been supported
249 by statistical analyses of seismic observations (Cobden et al., 2012, 2015) and by
250 comparisons between seismic tomography and geodynamic models (Koelemeijer et al.,
251 2018). Mineral physics models with post-perovskite are compatible with both global and
252 local seismic data of S- and P-wave velocity perturbations in the lowermost mantle rather
253 than post-perovskite-free models. Recent high-quality seismological data indicate that
254 non-observations of a discontinuity in the lowermost mantle are not common but
255 exceptional (Jackson & Thomas, 2021).

256 The ubiquitous presence of post-perovskite above the CMB has profound geodynamical
257 consequences. Because of its proximity to the CMB, the global occurrence of the
258 bridgmanite/post-perovskite phase transition with high positive Clapeyron slope ($+7^{+2}_{-3}$
259 MPa/K) destabilizes the thermal boundary layer developed at the bottom of the mantle
260 and enhances plume upwelling (Nakagawa & Tackley, 2004; Li et al., 2014; Hirose et al.,
261 2015). Theoretical calculations and experiments demonstrated that post-perovskite is at
262 least five times weaker than bridgmanite (Hunt et al., 2009; Ammann et al., 2010). The
263 low-viscosity D'' layer allows cold slab materials to spread extensively above the CMB,
264 leading to an increase in heat transfer from the core (Buffett, 2007; Cizkova et al., 2010).
265 It also enhances the segregation of MORB crust materials from the rest of the subducted
266 slab, contributing to the formation of dense piles above the CMB (Nakagawa & Tackley,
267 2011).

268 Ultralow-velocity zones are observed locally above the CMB, likely representing
269 partially molten materials with relatively low melting temperatures such as FeO-rich ones
270 (Boukaré et al., 2015; Helffrich et al., 2020). On the other hand, when the CMB
271 temperature was higher in the past (Labrosse, 2015), the lowermost mantle could have
272 been globally molten. The present experiments demonstrate that post-perovskite is the
273 liquidus phase (the first phase to appear upon crystallization) in a pyrolitic lowermost
274 mantle (Tateno et al., 2014) (Figure 3). The behaviors of trace elements during partial
275 melting involving post-perovskite may be different from that with bridgmanite at
276 shallower depths; water and Na₂O have been shown to be partitioned more into Al-
277 bearing post-perovskite than into bridgmanite (Townsend et al., 2016; Hirose et al., 2005;
278 Tateno et al., 2018b). Partitioning of trace elements between melt and post-perovskite is
279 yet to be explored.

280 5. Conclusions

281 We have examined the phase transition between bridgmanite and post-perovskite in a
282 pyrolitic mantle material at high temperatures (3570–4480 K) around the CMB pressure.
283 Results demonstrate that the bridgmanite/post-perovskite phase transition occurs in
284 pyrolite within the lowermost mantle pressure range even at >4000 K. They also indicate
285 the two-phase coexisting region of ~5 GPa and the Clapeyron slope of $+7\pm_3^2$ MPa/K,
286 when combined with earlier experimental results obtained at lower temperatures (Ohta et
287 al., 2008).

288 The global presence of post-perovskite above the CMB is consistent with recent high-
289 quality seismological observations of the D'' seismic reflections; they are found not only
290 in the circum-Pacific high-velocity regions but also in many places away from such
291 (presumably) cold areas (Jackson & Thomas, 2021). The 5 GPa two-phase coexisting
292 interval may be too thick for the bridgmanite/post-perovskite phase transition in pyrolite
293 to be the cause of seismic reflections. Alternatively the seismic discontinuity observed
294 underneath subduction zones could be attributed to the post-perovskite phase transition
295 in depleted peridotite materials that should be abundant in such areas (Grocholski et al.,
296 2012) or caused by scattering off chemical heterogeneities that derive from subductions
297 of former oceanic plates (Cobden & Thomas, 2013). The D'' reflections observed in areas
298 distant from subduction zones can be formed by other mechanisms such as deformation
299 of weak post-perovskite within a two-phase region (Ammann et al., 2010; Pisconti et al.,
300 2019). Indeed, the ubiquitous occurrence of post-perovskite above the CMB is supported
301 by a statistical interpretation of seismic observations (Cobden et al., 2012, 2015) and by

302 comparisons of seismic tomographies between observed and synthesized from
303 geodynamic simulations (Koelemeijer et al., 2018). The global presence of rheologically
304 weak post-perovskite at the bottom of the mantle has profound implications for the
305 dynamics and thermal histories of both the mantle and the core.

306 **Data Availability Statement**

307 Datasets for this research are found in [Table 1](#) available online (from
308 <https://zenodo.org/record/5513281>).

309 **Acknowledgments**

310 K. Yonemitsu is acknowledged for her help in FIB/SEM/EDS analyses. XRD
311 measurements were carried out at BL10XU, SPring-8 (proposals no. 2019B0072 and
312 2020A0072). This work was supported by the JSPS grants 16H06285 and 21H04968 to
313 K.H.

314 **References**

- 315 Ammann, M. W., Brodholt, J. P., Wookey, J., & Dobson, D. P. (2010). First-principles
316 constraints on diffusion in lower-mantle minerals and a weak D'' layer. *Nature*, *465*,
317 462–465. <http://dx.doi.org/10.1038/nature09052>
- 318 Anderson, O. L., Isaak, D. G., & Yamamoto, S. (1989). Anharmonicity and the equation
319 of state for gold. *Journal of Applied Physics*, *65*, 1534–1543.
320 <https://doi.org/10.1063/1.342969>
- 321 Andrault, D., Muñoz, M., Bolfan-Casanova, N., Guignot, N., Perrillat, J.-P., Aquilanti,
322 G., & Pascarelli, S. (2010). Experimental evidence for perovskite and post-perovskite
323 coexistence throughout the whole D'' region. *Earth and Planetary Science Letters*,
324 *293*, 90–96. <https://doi.org/10.1016/j.epsl.2010.02.026>
- 325 Boukaré, C.-E., Ricard, Y., & Fiquet, G. (2015). Thermodynamics of the MgO-FeO-SiO₂
326 system up to 140 GPa: application to the crystallization of Earth's magma ocean.
327 *Journal of Geophysical Research: Solid Earth*, *120*, 6085–6101.
328 <https://doi.org/10.1002/2015JB011929>
- 329 Brown, M. J., & Shankland, T. J. (1981). Thermodynamic parameters in the Earth as
330 determined from seismic profiles. *Geophysical Journal Royal Astronomical Society*,
331 *66*, 579–596.

- 332 Buffett, B. A. (2007). A bound on heat flow below a double crossing of the perovskite-
333 postperovskite phase transition. *Geophysical Research Letters*, *34*, L17302.
334 doi:10.1029/2007GL030930
- 335 Catalli K., Shim S. H., & Prakapenka, V. (2009). Thickness and Clapeyron slope of the
336 post-perovskite boundary. *Nature*, *462*, 782–785.
337 <https://doi.org/10.1038/nature08598>
- 338 Cizkova, H., Cadek, O., Matyska, C., & Yuen, D. A. (2010). Implications of post-
339 perovskite transport properties for core–mantle dynamics. *Physics of Earth and*
340 *Planetary Interiors*, *180*, 235–243. <https://doi.org/10.1016/j.pepi.2009.08.008>
- 341 Cobden, L., & Thomas, C. (2013). The origin of D'' reflections: a systematic study of
342 seismic array data sets. *Geophysical Journal International*, *194*, 1091–1118.
343 <https://doi.org/10.1093/gji/ggt152>
- 344 Cobden, L., Mosca, I., Trampert, J., & Ritsema, J. (2012). On the likelihood of post-
345 perovskite near the core-mantle boundary: a statistical interpretation of seismic
346 observations. *Physics of the Earth and Planetary Interiors*, *210–211*, 21–35.
347 <http://dx.doi.org/10.1016/j.pepi.2012.08.007>
- 348 Cobden, L., Thomas, C., & Trampert, J. (2015). Seismic detection of post-perovskite
349 inside the Earth. In A. Khan, F. Deschamps (Eds.), *The Earth's Heterogeneous*
350 *Mantle* (pp. 391–440). Switzerland: Springer Geophysics. DOI: 10.1007/978-3-319-
351 15627-9_13
- 352 Fei, Y., Ricolleau, A., Frank, M., Mibe, K., Shen, G., & Prakapenka, V. (2007) . Toward
353 an internally consistent pressure scale. *Proceedings of the National Academy of*
354 *Sciences of the United States of America*, *104*, 9182–9186.
355 <https://doi.org/10.1073/pnas.0609013104>
- 356 Fiquet, G., Auzende, A. L., Siebert, J., Corgne, A., Bureau, H., Ozawa, H., & Garbarino,
357 G. (2010). Melting of peridotite to 140 Gigapascals. *Science*, *329*, 1516–1518. DOI:
358 10.1126/science.1192448
- 359 Grocholski, B., Catalli, K., Shim, S-H., & Prakapenka, V. (2012). Mineralogical effects
360 on the detectability of the postperovskite boundary. *Proceedings of the National*
361 *Academy of Sciences of the United States of America*, *109*, 2275–
362 2279. <https://doi.org/10.1073/pnas.1109204109>
- 363 Hasegawa, M., Hirose, K., Oka, K., & Ohishi, Y. (2021). Liquidus phase relations and
364 solid-liquid partitioning in the Fe-Si-C system under core pressures. *Geophysical*
365 *Research Letters*, *48*, e2021GL092681. <https://doi.org/10.1029/2021GL092681>

366 Helffrich, G., Hirose, K., & Nomura, R. (2020). Thermodynamical modeling of liquid
367 Fe-Si-Mg-O: molten magnesium silicate release from the core. *Geophysical Research*
368 *Letters*, *47*, e2020GL089218. <https://doi.org/10.1029/2020GL089218>

369 Hernlund, J. W., Thomas, C., & Tackley, P. J. (2005). A doubling of the postperovskite
370 phase boundary and structure of the Earth's lower mantle. *Nature*, *434*, 882–886.
371 <https://doi.org/10.1038/nature03472>

372 Hirao, N., Kawaguchi, S., Hirose, K., Shimizu, K., Ohtani, E., & Ohishi, Y. (2020). New
373 developments in high-pressure X-ray diffraction beamline for diamond anvil cell at
374 SPring-8. *Matter and Radiation at Extremes*, *5*, 018403.
375 <https://doi.org/10.1063/1.5126038>

376 Hirose, K., Takafuji, N., Sata, N., & Ohishi, Y. (2005). Phase transition and density of
377 subducted MORB crust in the lower mantle. *Earth and Planetary Science Letters*, *237*,
378 239–251. <http://dx.doi.org/10.1016/j.epsl.2005.06.035>

379 Hirose, K., Sinmyo, R., Sata, N., & Ohishi, Y. (2006). Determination of post-perovskite
380 phase transition boundary in MgSiO₃ using Au and MgO internal pressure standards.
381 *Geophysical Research Letters*, *33*, L01310.
382 <http://dx.doi.org/10.1029/2005GL024468>

383 Hirose, K., Takafuji, N., Fujino, K., Shieh, S. R., & Duffy, T. S., (2008). Iron partitioning
384 between perovskite and post-perovskite: A transmission electron microscope study.
385 *American Mineralogist*, *93*, 1678–1681. <http://dx.doi.org/10.2138/am.2008.3001>

386 Hirose, K., Sata, N., Komabayashi, T., & Ohishi, Y. (2008). Simultaneous volume
387 measurements of Au and MgO to 140 GPa and thermal equation of state of Au based
388 on MgO pressure scale. *Physics of the Earth and Planetary Interiors*, *167*, 149–154.
389 <https://doi.org/10.1016/j.pepi.2008.03.002>

390 Hirose, K., Wentzcovitch, R., Yuen, D., & Lay, T. (2015). Mineralogy of the deep mantle
391 – the post-perovskite phase and its geophysical significance. In G. Schubert (Ed.),
392 *Treatise on Geophysics*, 2nd edition (Vol. 2, pp. 85–115). Oxford: Elsevier.
393 <https://doi.org/10.1016/B978-0-444-53802-4.00054-3>

394 Hunt, S. A., Weidner, D. J., Li, L., Wang, L., Walte, N. P., Brodholt, J. P., & Dobson, D.
395 P. (2009). Weakening of calcium iridate during its transformation from perovskite to
396 post-perovskite. *Nature Geosciences*, *2*, 794–797. DOI: 10.1038/NGEO663

397 Jackson, J. M., & Thomas, C. (2021). Seismic and mineral physics constraints on the D''
398 Layer. In H. Marquardt, M. Ballmer, S. Cottaar, J. Konter (Eds.), *Mantle convection*
399 *and surface expressions*, *Geophysical Monograph Series* (Vol. 263, pp. 193–227).
400 Washington, DC: John Wiley & Sons, Inc. DOI: 10.1002/9781119528609.ch8

- 401 Jamieson, J. C., Fritz, J. N., & Manghnani, M. H. (1982). Pressure measurement at high
402 temperature in x-ray diffraction studies: gold as a primary standard. In S. Akimoto,
403 M.H. Manghnani (Eds.), *High-pressure research in geophysics* (pp. 27–48). Tokyo:
404 CAPJ.
- 405 Kim, T., Ko, B., Greenberg, E., Prakapenka, V., Shim, S-H., & Lee, Y. (2020). Low
406 melting temperature of anhydrous mantle materials at the core-mantle boundary.
407 *Geophysical Research Letters*, *47*, e2020GL089345.
408 <https://doi.org/10.1029/2020GL089345>
- 409 Koelemeijer, P., Schuberth, B. S. A., Davies, D. R., Deuss, A., & Ritsema, J. (2018).
410 Constraints on the presence of post-perovskite in Earth's lowermost mantle from
411 tomographic-geodynamic model comparisons. *Earth and Planetary Science Letters*,
412 *494*, 226–238. <https://doi.org/10.1016/j.epsl.2018.04.056>
- 413 Labrosse, S. (2015). Thermal evolution of the core with a high thermal conductivity.
414 *Physics of the Earth and Planetary Interiors*. *247*, 36–55.
415 <https://doi.org/10.1016/j.pepi.2015.02.002>
- 416 Langrand, C., Andraut, D., Durand, S., Konôpková, Z., Hilairret, N., Thomas, C., &
417 Merkel, S. (2019). Kinetics and detectability of the bridgmanite to post-perovskite
418 transformation in the Earth's D'' layer. *Nature communications*, *10*, 5680.
419 <https://doi.org/10.1038/s41467-019-13482-x>
- 420 Lay, T. (2008). Sharpness of the D'' discontinuity beneath the Cocos Plate: implications
421 for the perovskite to post-perovskite phase transition. *Geophysical Research Letters*,
422 *35*, L03304. <http://dx.doi.org/10.1029/2007GL032465>
- 423 Lay, T. & Young, C. J. (1989). Waveform complexity in teleseismic broadband SH
424 displacements: Slab diffractions or deep mantle reflections? *Geophysical Research*
425 *Letters*, *16*, 605–608.
426 [https://deepblue.lib.umich.edu/bitstream/handle/2027.42/95458/grl4356.pdf?sequen](https://deepblue.lib.umich.edu/bitstream/handle/2027.42/95458/grl4356.pdf?sequence=1&isAllowed=y)
427 [ce=1&isAllowed=y](https://deepblue.lib.umich.edu/bitstream/handle/2027.42/95458/grl4356.pdf?sequence=1&isAllowed=y)
- 428 Lay, T., Hernlund, J., Garnero, E. J., & Thorne, S. (2006) . A post-perovskite lens and D''
429 heat flux beneath the central Pacific. *Science*, *314*, 1272–1276.
430 DOI: 10.1126/science.1133280
- 431 Lay, T., Hernlund, J., & Buffett, B. A. (2008). Core–mantle boundary heat flow. *Nature*
432 *Geoscience*, *1*, 25–32. DOI:10.1038/ngeo.2007.44
- 433 Li, Y., Deschamps, F. & Tackley, P. J. (2014). Effects of low-viscosity post-perovskite
434 on the stability and structure of primordial reservoirs in the lower mantle. *Geophysical*
435 *Research Letters*, *41*, 7089–7097. doi: 10.1002/2014GL061362

436 Mao, W. L., Meng, Y., Shen, G., Prakapenka, V. B., Campbell, A. J., Heinz, et al. (2005).
437 Iron-rich silicates in the Earth's D'' layer. *Proceedings of the National Academy of*
438 *Sciences of the United States of America*, 102, 9751–9753.
439 doi: 10.1073/pnas.0503737102

440 Mashino, I., Murakami, M., Miyajima, N., & Petitgirard, S. (2020). Experimental
441 evidence for silica–enriched Earth's lower mantle with ferrous iron dominant
442 bridgmanite. *Proceedings of the National Academy of Sciences of the United States*
443 *of America*, 117, 27899–27905. <https://doi.org/10.1073/pnas.1917096117>

444 Mori, Y., Ozawa, H., Hirose, K., Sinmyo, R., Tateno, S., Morard, G., & Ohishi, Y. (2017).
445 Melting experiments on Fe–Fe₃S system to 254 GPa. *Earth and Planetary Science*
446 *Letters*, 464, 135–141. <https://doi.org/10.1016/j.epsl.2017.02.021>

447 Murakami, M., Hirose, K., Kawamura, K., Sata, N., & Ohishi, Y. (2004). Post-perovskite
448 phase transition in MgSiO₃. *Science*, 304, 855–858. DOI:10.1126/science.1095932

449 Murakami, M., Hirose, K., Sata, N., & Ohishi, Y. (2005). Post-perovskite phase transition
450 and crystal chemistry in the pyrolitic lowermost mantle. *Geophysical Research*
451 *Letters*, 32, L03304. <http://dx.doi.org/10.1029/2004GL021956>

452 Murakami, M., Ohishi, Y., Hirao, N., & Hirose, K. (2012). A perovskitic lower mantle
453 inferred from high-pressure, high-temperature sound velocity data. *Nature*, 485, 90–
454 94. <https://doi.org/10.1038/nature11004>

455 Nakagawa, T. & Tackley, P. J. (2004). Effects of a perovskite–post perovskite phase
456 change mantle boundary in compressible mantle. *Geophysical Research Letters*, 31,
457 L16611. <http://dx.doi.org/10.1029/2004GL020648>

458 Nakagawa, T. & Tackley, P. J. (2011). Effects of low-viscosity post-perovskite on
459 thermo- chemical mantle convection in a 3-D spherical shell. *Geophysical Research*
460 *Letters*, 38, L04309. <http://dx.doi.org/10.1029/2010GL046494>

461 Nomura, R., Hirose, K., Uesugi, K., Ohishi, Y., Tsuchiyama, A., Miyake, A., & Ueno, Y.
462 (2014). Low core-mantle boundary temperature inferred from the solidus of pyrolite.
463 *Science*, 343, 522–525. DOI: 10.1126/science.1248186

464 Oganov, A. R. & Ono, S. (2004). Theoretical and experimental evidence for a post-
465 perovskite phase of MgSiO₃ in Earth's D'' layer. *Nature*, 430, 445–448.
466 DOI: 10.1038/nature02701

467 Ohta, K., Hirose, K., Lay, T., Sata, N., & Ohishi, Y. (2008). Phase transitions in pyrolite
468 and MORB at lowermost mantle conditions: Implications for a MORB-rich pile above
469 the core-mantle boundary. *Earth and Planetary Science Letters*, 267, 107–117.
470 <https://doi.org/10.1016/j.epsl.2007.11.037>

- 471 Ono, S. & Oganov, A. R. (2005). In situ observations of phase transition between
472 perovskite and CaIrO₃-type phase in MgSiO₃ and pyrolitic mantle composition. *Earth
473 and Planetary Science Letters*, 236, 914–932. DOI:10.1016/j.epsl.2005.06.001
- 474 Pisconti, A., Thomas, C., & Wookey, J. (2019). Discriminating between causes of D''
475 anisotropy using reflections and splitting measurements for a single path. *Journal of
476 Geophysical Research: Solid Earth*, 124, 4811–4830. [https://doi.org/10.1029/
477 2018JB016993](https://doi.org/10.1029/2018JB016993)
- 478 Seto, Y., Nishio-Hamane, D., Nagai, T., & Sata, N. (2010). Development of a software
479 suite on X-ray diffraction experiments. *Review of High Pressure Science and
480 Technology*, 20, 269–276. <https://doi.org/10.4131/jshpreview.20.269>
- 481 Shim, S., Duffy, T. S., & Takemura, K. (2002). Equation of state of gold and its
482 application to the phase boundaries near 660 km depth in the Earth's mantle. *Earth
483 and Planetary Science Letters*, 203, 729–739. [https://doi.org/10.1016/S0012-
484 821X\(02\)00917-2](https://doi.org/10.1016/S0012-821X(02)00917-2)
- 485 Sinmyo, R., Hirose, K., Muto, S., Ohishi, Y., & Yasuhara, A. (2011). The valence state
486 and partitioning of iron in the Earth's lowermost mantle. *Journal of Geophysical
487 Research*, 116, B07205. <http://dx.doi.org/10.1029/2010JB008179>
- 488 Speziale, S., Zha, C., Duffy, T.S., Hemley, R. J., & Mao, H. K. (2001). Quasi-hydrostatic
489 compression of magnesium oxide to 52 GPa: implications for the pressure–volume–
490 temperature equation of state. *Journal of Geophysical Research*, 106, 515–528.
491 <https://doi.org/10.1029/2000JB900318>
- 492 Tackley, P. J., Nakagawa, T., & Hernlund, J. W. (2007). Influence of the post-perovskite
493 transition on thermal and thermo-chemical mantle convection. In K. Hirose, J.
494 Brodholt, T. Lay, D. Yuen (Eds.), *Post-perovskite: the last mantle phase transition*,
495 *Geophysical Monograph Series* (Vol. 174, pp. 229–247). Washington, DC: American
496 Geophysical Union. <http://dx.doi.org/10.1029/174GM11>
- 497 Takahashi, E. (1986). Melting of a dry peridotite KLB-1 up to 14 GPa: implications on
498 the origin of peridotite upper mantle. *Journal of Geophysical Research*, 91, 9367–
499 9382. <https://doi.org/10.1029/JB091iB09p09367>
- 500 Tateno, S., Hirose, K., Sata, N., & Ohishi, Y. (2005). Phase relations in Mg₃Al₂Si₃O₁₂ to
501 180 GPa: effect of Al on post-perovskite phase transition. *Geophysical Research
502 Letters*, 32, L15306. <http://dx.doi.org/10.1029/2005GL023309>
- 503 Tateno, S., Hirose, K., Sata, N., & Ohishi, Y. (2009). Determination of post-perovskite
504 phase transition boundary up to 4,400 K and implications for thermal structure in D''
505 layer. *Earth and Planetary Science Letters*, 277, 130–136.
506 <https://doi.org/10.1016/J.EPSL.2008.10.004>

507 Tateno, S., Hirose, K., & Ohishi, Y. (2014). Melting experiments on peridotite to
508 lowermost mantle conditions. *Journal of Geophysical Research: Solid Earth*, *119*,
509 4684–4694. <https://doi.org/10.1002/2013JB010616>

510 Tateno, S., Hirose, K., Sinmyo, R., Morard, G., Hirao, N., & Ohishi, Y. (2018a). Melting
511 of Fe–Si–S alloys to core pressures: silicon in the core? *American Mineralogist*, *103*,
512 742–748. <https://doi.org/10.2138/am-2018-6299>

513 Tateno, S., Hirose, K., Sakata, S., Yonemitsu, K., Ozawa, H., Hirata, T., et al. (2018b).
514 Melting phase relations and element partitioning in MORB to lowermost mantle
515 conditions. *Journal of Geophysical Research: Solid Earth*, *123*,
516 <https://doi.org/10.1029/2018JB015790>

517 Thomas, C., Kendall, J. M., & Lowman, J. (2004b). Lower-mantle seismic discontinuities
518 and the thermal morphology of subducted slabs. *Earth and Planetary Science Letters*,
519 *225*, 105–113. doi:10.1016/j.epsl.2004.05.038

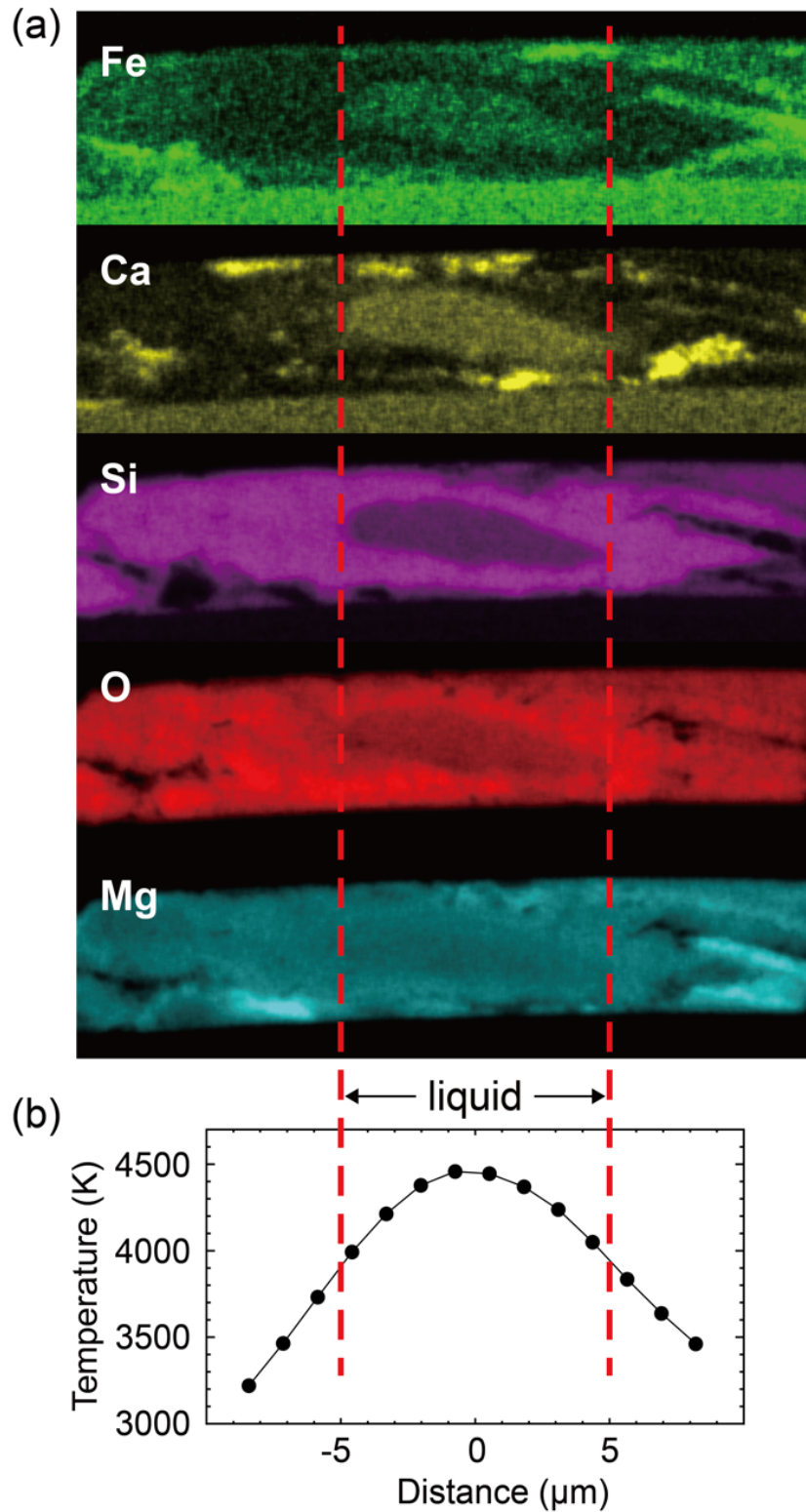
520 Townsend, J. P., Tsuchiya, J., Bina, C. R., & Jacobsen, S. D. (2016). Water partitioning
521 between bridgmanite and postperovskite in the lowermost mantle. *Earth and*
522 *Planetary Science Letters*, *454*, 20–27. <http://dx.doi.org/10.1016/j.epsl.2016.08.009>

523 Tsuchiya, T., (2003). First-principles prediction of the P – V – T equation of state of gold
524 and the 660-km discontinuity in Earth’s mantle. *Journal of Geophysical Research*,
525 *108*, <https://doi.org/10.1029/2003JB002446>

526 Tsuchiya, T., Tsuchiya, J., Umemoto, K., & Wentzcovitch, R. M. (2004). Phase transition
527 in MgSiO₃ perovskite in the Earth’s lower mantle. *Earth and Planetary Science*
528 *Letters*, *224*, 241–248. <https://doi.org/10.1016/j.epsl.2004.05.017>

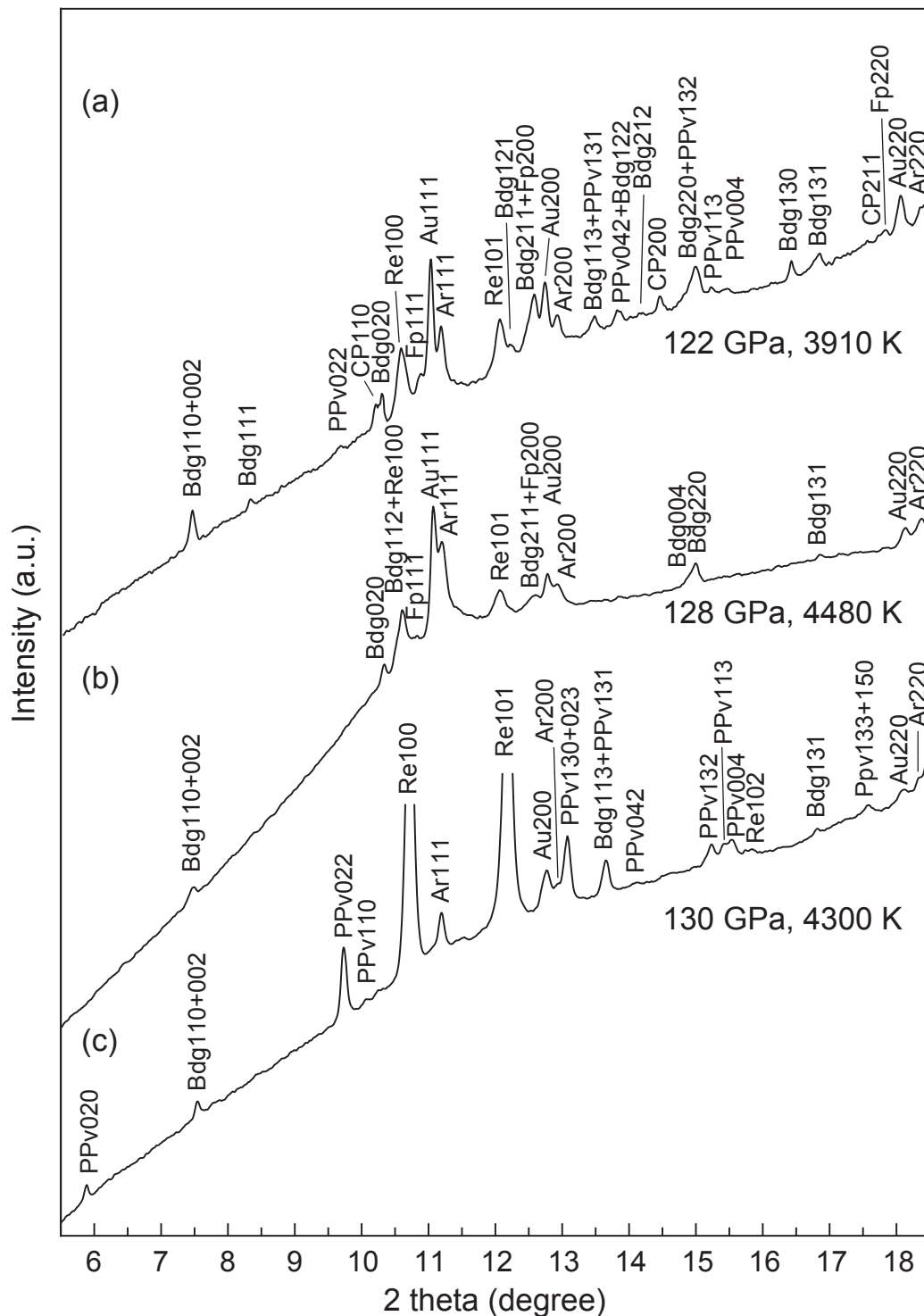
529 Weber, M., Davis, J. P., Thomas, C., Krüger, F., Scherbaum, F., Schlittenhardt, J., &
530 Körnig, M. (1996). The structure of the lowermost mantle as determined from using
531 seismic arrays. In E. Boschi, G. Ekström, A. Morelli (Eds.), *Seismic modelling of the*
532 *Earth’s structure* (pp. 399–442). Rome: Istituto Nazionale di Geophysica.

533 Wyssession, M. E., Lay, T., Revenaugh, J., Williams, Q., Garnero, E. J., Jeanloz, R.,
534 Kellogg, L. H. (1998). The D” discontinuity and its implications. In M. Gurnis, M.E.
535 Wyssession, E. Knittle, B.A. Buffett (Eds.), *The core-mantle boundary region*,
536 *Geodynamical Series* (Vol. 28, pp. 273–297). Washington, DC: American
537 Geophysical Union.



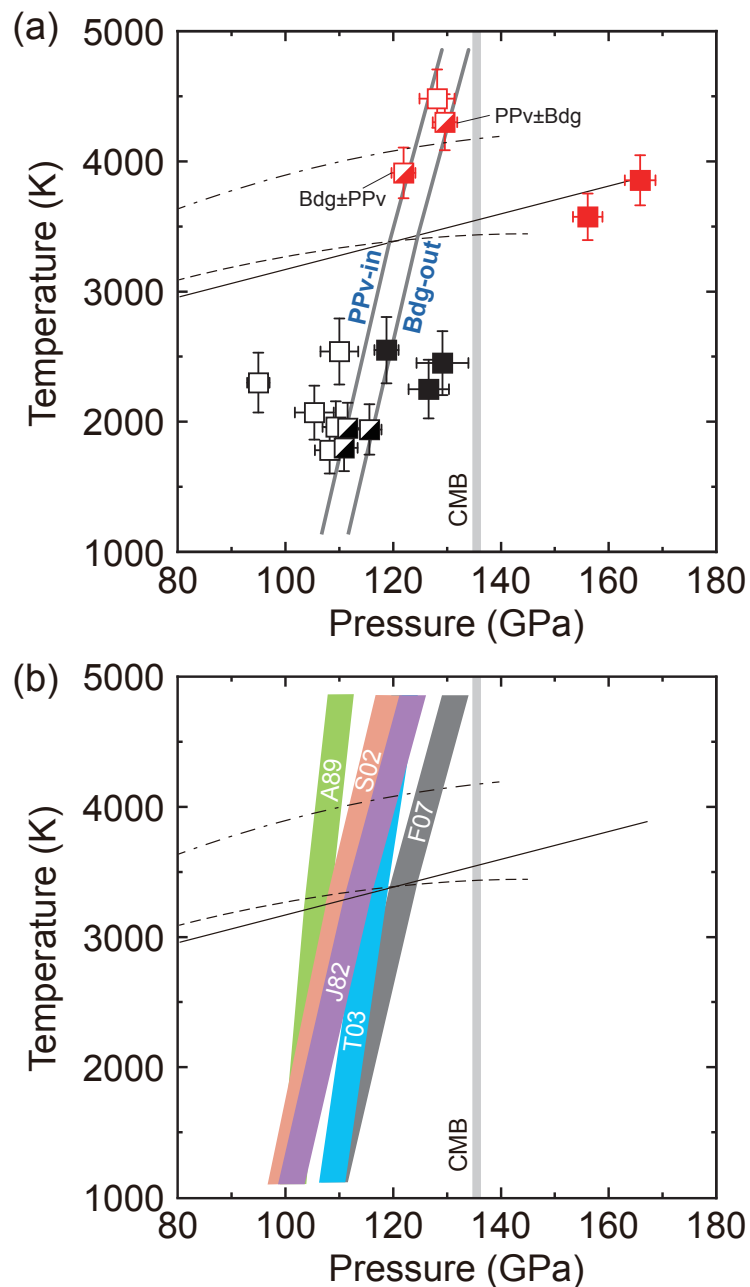
538

539 **Figure 1.** (a) X-ray elemental maps of the sample cross section recovered from run #1 at
 540 122 GPa and 3910 K. (b) A corresponding temperature profile across the hot spot.



541

542 **Figure 2.** X-ray diffraction patterns at (a) 122 GPa and 3910 K, (b) 128 GPa and 4480 K,
 543 and (c) 130 GPa and 4300 K. Bdg, MgSiO₃-rich perovskite; PPv, post-perovskite; Fp,
 544 ferropericlasite; CP, CaSiO₃ perovskite; Au, gold; Ar, argon pressure medium; Re,
 545 rhenium gasket.



546

547 **Figure 3.** (a) Phase boundary between bridgmanite (Bdg) and post-perovskite (PPv).
 548 Open and solid symbols represent the stabilities of bridgmanite and post-perovskite,
 549 respectively. Half-filled symbols show the coexistence of both phases. Red symbols, this
 550 study; black symbols, from Ohta et al. (2008). Solid, broken, and dashed-dotted curves
 551 indicate solidus temperatures of pyrolite reported by Nomura et al. (2014), Kim et al.
 552 (2020), and Fiquet et al. (2010), respectively. (b) Changes in the phase boundary by using
 553 different EoS of gold to calculate experimental pressures (Jamieson et al., 1982;
 554 Anderson et al., 1989; Shim et al., 2002; Tsuchiya, 2003; Fei et al., 2007).

555

556 **Table 1**557 *Experimental Results*

Run#	Volume of Au (Å ³)	Pressure (GPa)	Temperature (K)	Phase assemblage
<i>This study</i>				
#1	52.19(5)	121.9(2)	3910	Bdg + PPv (trace) + Fp + CaPv + melt
#2	52.06(12)	128.1(3)	4480	Bdg + Fp + melt
#3	51.82(4)	129.6(2)	4300	PPv + Bdg (trace) + melt
#4	49.08(8)	165.9(3)	3860	PPv + Fp + CaPv
#5	49.53(8)	156.1(3)	3570	PPv + Fp + CaPv
<i>Ohta et al. (2008)</i>				
#1-1	51.91(11)	108.2(3)	1780	Bdg + Fp + CaPv
#1-2	51.93(7)	109.4(2)	1960	Bdg + Fp + CaPv
#1-3	52.26(12)	110.0(3)	2540	Bdg + Fp + CaPv
#2-1	51.70(8)	110.9(2)	1800	Bdg + PPv (trace) + Fp + CaPv
#2-2	51.75(9)	111.6(3)	1950	Bdg + PPv (trace) + Fp + CaPv
#3	51.43(6)	115.6(2)	1940	PPv + Bdg + Fp + CaPv
#4	53.43(3)	95.0(2)	2300	Bdg + Fp + CaPv
#5	52.33(17)	105.4(3)	2070	Bdg + Fp + CaPv
#6	51.56(1)	118.8(2)	2550	PPv + Fp + CaPv
#7	50.79(14)	126.6(4)	2250	PPv + Fp + CaPv
#8	50.72(20)	129.1(4)	2450	PPv + Fp + CaPv

The numbers in parentheses represent one standard deviation in the last digits.

Bdg, bridgmanite; PPv, post-perovskite; Fp, ferropericlase; CaPv, CaSiO₃ perovskite

558